RESEARCH ARTICLE

NANO · MICRO small
www.small-journal.com

Efficient Humidity-to-Hydrogen Photocatalysis: Engineering Polymer-Catalyst Bonds in Hygroscopic Hydrogels with Sulfur-Vacancy-Rich Nanosheets

*Zhen Liu, Liangyu Li, Huping Yan, Chuanshuai Dong, Mengying Li, and Ronghui Qi**

This study presents an efficient hydrogel-based photocatalytic system for green hydrogen production directly from atmospheric humidity. By constructing a triangular-pyramid Zn-O bonding structure between hygroscopic polyacrylamide (PAM) hydrogel and sulfur vacancy-rich $ZnIn_2S_4$ (Sv-ZIS) nanosheets, strong interactions between gel O atoms and Zn atoms near S vacancies lead to shorter, more stable bonds. This structure enhances charge separation, accelerates reactant and product transport, and reinforces the hydrogel's mechanical properties. The composite achieves an apparent quantum efficiency of 35.1% at 365 nm and a stable hydrogen evolution rate of 28.79 mmol/gcat/h at ∼30 °C and 50% RH under 100 mW cm^{-2} irradiation — surpassing traditional water-based photocatalysis. It also performs well under low-intensity LED light, indicating potential for indoor use. Molecular dynamics and DFT simulations reveal that the pyramid structure promotes polymer chain extension, increases water binding sites, and that sulfur vacancies facilitate H* desorption and further strengthen Zn-O interactions. The synergistic effect of the polymer matrix and sulfur vacancies boosts both activity and durability, while maintaining hygroscopicity. The composite is prepared via a mild, scalable in-situ method, highlighting its potential for practical, sustainable hydrogen production from ambient moisture.

1. Introduction

Photocatalysis is an important technology converting light into chemical energy.[1–3] Current photocatalytic systems mainly target water splitting, often requiring additional sacrificial agents alongside catalysts due to the low overall water splitting efficiency. However, this process faces challenges such as water pollution caused by adding catalytic powders, dependence on fresh water, and reduction of photocatalyst active surfaces caused by bubble adhesion.[4–7] Photocatalytic hydrogen production utilizing water vapor offers great scalability in recent years.[8–10] This technology can harness moisture from air or water evaporation and aids in humidity control, which is ideal for regions with scarce freshwater and high humidity, such as coastal areas. Besides, it can utilize steam discharged from thermal, nuclear, and chemical power plants for hydrogen production. This water-independent hydrogen production technology is ideal for deserts, as it uses humid air instead of scarce liquid water to produce hydrogen efficiently. Additionally, it promotes clean energy development by offering a sustainable and eco-friendly method to generate hydrogen, a key fuel for reducing reliance on fossil fuels.

Recent studies have highlighted the hydrogels as a promising supporting material for vapor-based photocatalysis.[11,12] These transparent and hygroscopic chain-like polymer materials can be easily fabricated to have a uniform microstructure with well-organized gel network, suitable for supporting catalysts and additives, promoting their dispersion and preventing water pollution.[13,14] The hydrogel's network structure also regulates the water layers on the catalyst attached to the polymer chains, ensuring that the catalyst surface is moist and promotes H^+ migration without being too thick to hinder gas diffusion. Thus, this system can exhibit higher hydrogen diffusion rates[15–19] and promote the rapid departure of bubbles.[20] Additionally, hydrogels exhibit excellent hygroscopicity properties which can be attributed to their abundance of oxygen-containing functional groups (—OH, —COOH, etc.)[21,22] ensuring the moisture supply and avoiding the adverse effects of poor water quality on catalytic performance.

Selecting an appropriate photocatalyst is crucial for hydrogel-based setups. Recently, modification involving the bonding of photocatalysts with polymer molecules has drawn increasing attentions.[23,24] Nie et al.[25] indicated that polydimethylsiloxane can facilitate the formation of Ti-O-Si bonds between TiO_2 and $BaTiO_3$ semiconductor particles, serving as a channel for efficient charge carrier migration and subsequent effective charge

Z. Liu, L. Li, H. Yan, C. Dong, R. Qi
Key Laboratory of Enhanced Heat Transfer and Energy Conservation-Ministry of Education
School of Chemistry and Chemical Engineering
South China University of Technology
Guangzhou 510640, China
E-mail: qirh@scut.edu.cn

M. Li
Department of Mechanical Engineering
The Hong Kong Polytechnic University (PolyU)
Hong Kong SAR 999077, China

The ORCID identification number(s) for the author(s) of this article can be found under https://doi.org/10.1002/smll.202506127

DOI: 10.1002/smll.202506127

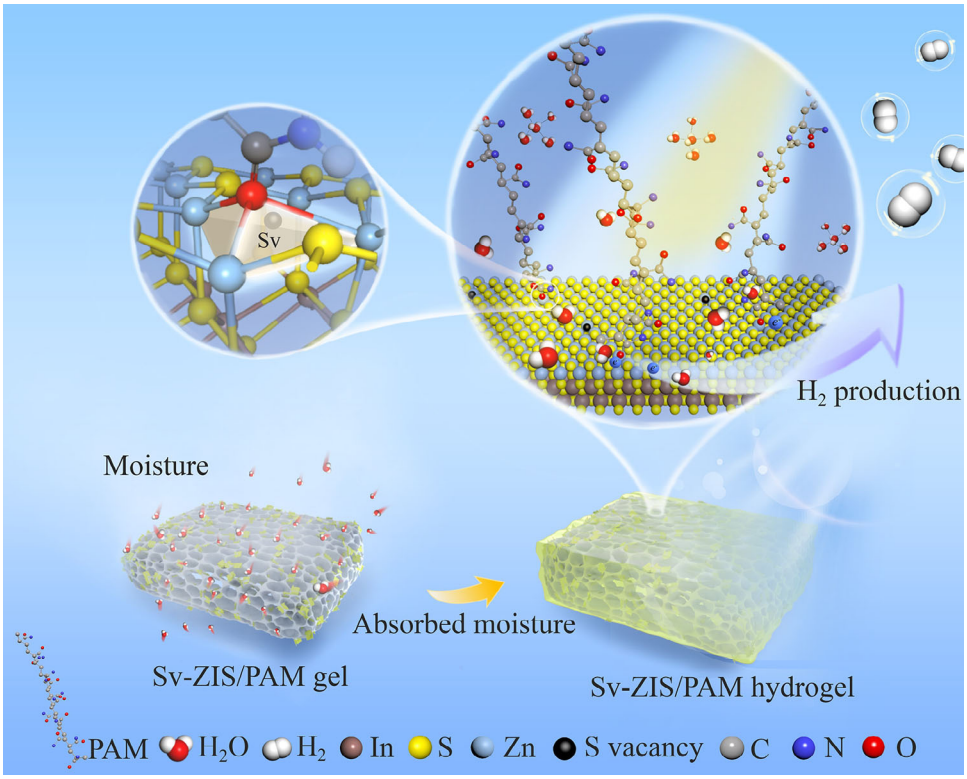

Figure 1. Schematic diagram of the sulfur vacancy-rich $ZnIn_2S_4$ nanosheet hydrogel photocatalysis and triangular pyramidal Zn-O bonding structure developed in this study.

separation. $ZnIn_2S_4$ shows promise due to its good activity, stability and visible-light-absorption,[26–29] and the sulfur sites in sulfides are regarded as active sites for the hydrogen evolution reaction due to their lower hydrogen adsorption free energy. To reduce the recombination of $ZnIn_2S_4$ photogenerated carriers and improve photocatalytic activity, modification strategies include the co-catalysts integration,[30–32] heteroatom doping,[33,34] and defects constructing[35,36] have been widely explored. Among these, sulfur vacancies are especially effective in tuning electronic properties, promoting charge separation, and enhancing surface catalytic activity. Recent studies reveal that sulfur vacancies in $ZnIn_2S_4$ nanosheets reduce hydrogen adsorption free energy and enhance the adsorption and activation of reactants, significantly boosting the performance of hydrogen evolution and other photocatalytic reactions.[37,38] Additionally, sulfur vacancies in modified $ZnIn_2S_4$ can induce polarization electric field and accelerate the transfer kinetics of carriers from the bulk phase to the surface redox sites, thereby improving the overall water splitting performance.[39–41]

Recent literature emphasized the benefits of incorporating hydrogels into photocatalytic systems, highlighting their ability to utilize the hygroscopic properties, structural adaptability, and physical confinement effects help improve catalyst dispersion and water capture, suggesting a promising avenue toward achieving efficient humidity-to-hydrogen conversion. Current hydrogel-based photocatalyst systems mainly focus on passive physical interactions, such as embedding or coating, overlooking the potential of optimizing the interactions between the hydrogel and catalyst to further enhance photocatalytic efficiency.

In contrast, this work introduces a rational interface engineering strategy based on the formation of Zn-O coordination bonds between the polymer chains and Sv-ZIS nanosheets, focusing on constructing internal triangular pyramidal polymer-photocatalyst linkages, as shown in **Figure 1**. Specifically, the Zn atoms near the sulfur vacancies form a triangular pyramid of Zn-O coordination bonds with the oxygen atoms of the carbonyl group in the PAM matrix. This interfacial structure strengthens charge transfer, improves polymer-catalyst coupling, and regulates the water microenvironment within the hydrogel. As a result, catalytically active intermediate water is selectively stabilized and more effectively decomposed, contributing to enhanced hydrogen evolution efficiency. Our approach combines experimental characterization with density functional theory (DFT) and molecular dynamics (MD) simulations to elucidate the critical role of pyramid-like bonds in exposing more active sites, promotes the retention and activation of intermediate water near the catalyst, and enhances the mechanical stability of the composite hydrogel. This comprehensive study provides fundamental understanding of the design of bonding interactions of hydrogel-based photocatalytic systems, and offers practical insights for sustainable hydrogen production.

2. Results and Discussion

2.1. Structural and Compositional Analysis of Hydrogel-Based Photocatalysts

First, Sv-ZIS nanosheets was successfully synthesized. As shown in Figure S5a,b (Supporting Information), both Sv-ZIS and ZIS samples exhibited a nanosheet morphology. The diameter of Sv-ZIS nanosheets was significantly reduced due to the adsorption of excess thioacetamide on the nanocrystals surface, which inhibited further growth.[42] The smaller size of Sv-ZIS nanosheets can lead to several advantages, including increased surface area and better dispersion. TEM and AFM analyses confirmed that Sv-ZIS formed an ultrathin 2D layered structure with a thickness of 1.26 nm (see supporting information for details, Figure S5c–e, Supporting Information). To better understand their photocatalytic performance, it is crucial to analyze the band edge positions. The semiconductor band edge positions, vital for photocatalytic reduction, were examined using Mott-Schottky plots, VB-XPS, and optical band gaps Figure S6a–e (Supporting Information).[43,44] The conduction band minimum of Sv-ZIS is −1.243 V and a valence band maximum is 1.097 V, and these values of ZIS are −1.033 and 1.187 V, respectively. The optical band gaps were estimated at 2.22 eV for ZIS and 2.34 eV for Sv-ZIS, indicating a minor difference in bandgap. However, the more negative CBM of Sv-ZIS compared to ZIS enhances its reduction capability, making it more effective for photocatalytic reduction reactions.[45]

Furthermore, with the nanosheet catalysts, a photocatalytic system using hygroscopic hydrogels polyacrylamide (PAM) was developed. The schematic illustration of the hydrogelation process was depicted in **Figure 2**a (see Figure S7, Supporting Information for a more detailed process). Figure S8 (Supporting Information) presents digital photographs of three hydrogel samples. The PAM hydrogel was transparent and colorless. The Sv-ZIS/PAM hydrogel displayed a uniformly transparent yellow color, while the ZIS/PAM hydrogel showed noticeable localized aggregated yellow regions at the bottom. The micromorphology surface structure of PAM, Sv-ZIS/PAM, and ZIS/PAM hydrogel with the inner porous structure constituted by the 3D interconnected network in Figure 2b–d. As shown in Figure 2e,f, the dried hydrogel of PAM and Sv-ZIS both exhibited smooth surface, indicating the Sv-ZIS were uniformly dispersed in PAM. The dried hydrogel of ZIS/PAM surface was very rough in Figure 2g, indicating the agglomeration of the polymer chain. The SEM-EDS mapping also verifies the uniform distribution of elements for Sv-ZIS/PAM in Figure 2h and Figure S9 (Supporting Information). The occurrence of this phenomenon is attributed to the interaction between the polymer chains and the catalyst during the synthesis of the photocatalysts-based hydrogel composite. A detailed discussion on this matter will be provided later in the subsequent sections.

Figure 2i shows the XRD pattern of the samples. The diffraction peak at $2\theta = 21.5°$, 27.5°, 30.5° and 47.3° can be assigned to (006), (102), (104) and (110) crystallographic planes of hexagonal $Znln_2S_4$ phase (PDF#65-2023). Compared to ZIS, the diffraction peak intensity of Sv-ZIS slightly decreases due to the presence of sulfur vacancies. The crystal structure of the hydrogel-based photocatalytic samples was investigated by XRD analysis after freeze-drying. Sv-ZIS/PAM and ZIS/PAM exhibited distinct characteristic peaks of both ZIS and PAM without other impurity peaks, indicating the presence of ZIS and PAM phases in the complexes. The slightly weaker characteristic of ZIS peaks in Sv-ZIS/PAM was due to low catalyst content. Only two broad peaks can be observed in PAM samples, due to its amorphous structure, which lacks a characteristic Bragg peak.[46] A physical mixture of Sv-ZIS and PAM was used as a control experiment (Figure S10, Supporting Information). The results show that although the diffraction peak positions of the composite sample and the physical mixture are similar, the changes in peak intensity and the increase in the amorphous background in the composite sample suggest that Sv-ZIS is well dispersed within PAM. Besides, the simplicity of preparation under ambient conditions suggests promising prospects for the large-scale production and application of this hydrogel photocatalytic material, with a production cost of ≈0.175 USD/g.

The surface compositions and chemical states of ZIS, Sv-ZIS, PAM, ZIS/PAM, and Sv-ZIS/PAM were studied by X-ray photoelectron spectroscopy (XPS), and the results are shown in **Figure 3**. In the XPS survey spectra (Figure S11a, Supporting Information), characteristic peaks corresponding to S, In, and Zn from ZIS, as well as C, N, and O from PAM, were observed in both ZIS/PAM and Sv-ZIS/PAM samples. No other elements were detected, confirming the successful incorporation of these components in the composite materials. For the spectrum of C 1s (Figure 3a), the peak at 284.8, 286.1, and 288.8 eV were assigned to the C—C, C—O—C and O—C═O in ZIS and Sv-ZIS, respectively.[47] And the peak at 287.8 eV attributed to N—C═O was also observed in the hydrogel samples.[48]

As mentioned before, the bonding interactions exited between the catalyst and the polymer chains. The presence of S vacancies in Sv-ZIS further enhanced its bonding with PAM, leading to optimal performance for Sv-ZIS/PAM. To better understand these interactions and the impact of S vacancies in electron transfer, we conducted a detailed XPS spectra analysis to elucidate the underlying charge redistribution mechanisms. As presented in Figure 3b, the 1 s spectrum of O in Sv-ZIS/PAM was deconvoluted into peaks of Zn-O, hydroxyl groups (OH^-) and absorbed H_2O, locating at 530.1, 531.6, and 533.1 eV.[34] In Figure 3c, the spectrum of S 2p in the samples can be fitted to two peaks, attributed to S^{2-}. The binding energy of S 2p of Sv-ZIS (S $2p_{1/2}$: 162.82 eV, S $2p_{3/2}$:161.65 eV) shifted to lower energy compared to ZIS (S $2p_{1/2}$: 162.99 eV, S $2p_{3/2}$: 161.78 eV), indicating increased electron attraction due to its higher electronegativity during the charge redistribution process induced by sulfur vacancies.[41] In the ZIS/PAM sample, the S 2p peak exhibited a shift toward lower binding energy compared to ZIS, attributed to the formation of Zn-O bonds. The electron density of the Zn atom is reduced and the charge was redistributed, thereby increasing the electron density of S atoms. For Sv-ZIS/PAM compared to Sv-ZIS, the S 2p peak of shifted to a higher binding energy, due to the presence of Zn-O bonding. The sulfur vacancies enhance the formation of Zn-O bond and lead to significant charge transfer. These binding energy changes highlight the critical role of PAM in regulating electron transfer and chemical bonding, with this interaction being particularly pronounced in the presence of sulfur vacancies.[49] Similar phenomenon was observed in Zn 2p (Figure S11b, Supporting Information) and In 3d (Figure S11c,

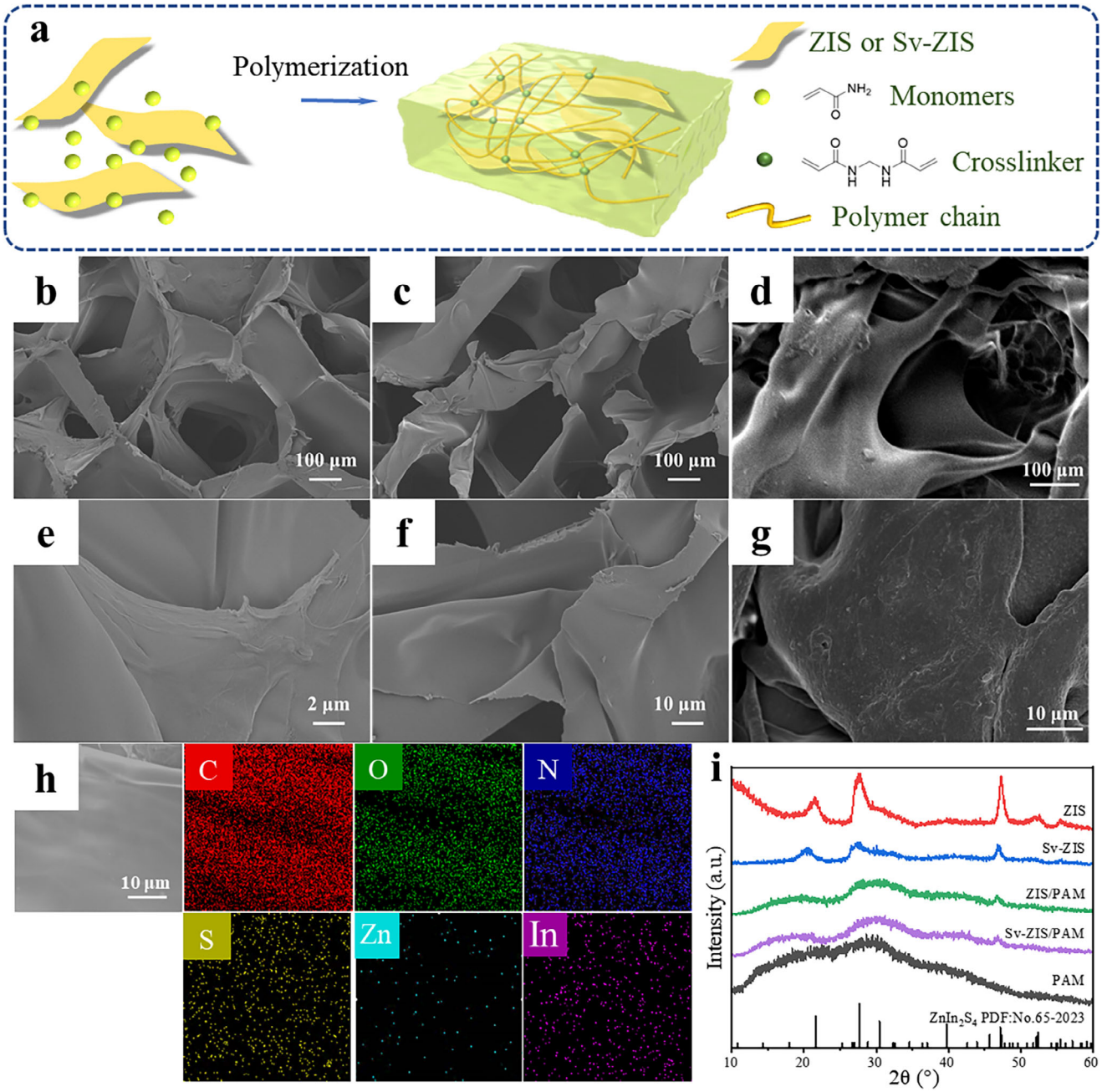

Figure 2. Characterization of hydrogel formation, morphology, and composition. a) Schematic route for hydrogelation. SEM of b,e) PAM, c,f) Sv-ZIS/PAM, d,g) ZIS/PAM. h) EDS-mapping for Sv-ZIS/PAM. i) XRD patterns of samples.

Supporting Information) as well. Zn 2p exhibited a larger shift toward lower binding energy (0.13 eV) compared to In 3d (0.05 eV). The shift in Zn 2p toward lower binding energy was more pronounced and closer to the 0.17 eV shift observed in S 2p, providing strong evidence that most sulfur vacancies are associated with Zn atoms rather than In atoms.[50]

The X-ray absorption fine structure spectroscopy (XAFS) at Zn K-edge was performed to further reveal the local atomic structures of the as-obtained samples, demonstrating the presence of Zn-O coordination in Sv-ZIS/PAM, as shown in Figure 3d–f. As shown in Figure 3d, the X-ray absorption near-edge structure (XANES) spectra of Zn K-edge manifest that the trend of adsorption threshold position was ZnO>Sv-ZIS/PAM>Sv-ZIS> Zn foil. Compared to Sv-ZIS, the pre-edge of Zn increased to a higher energy in Sv-ZIS/PAM. This was due to the charge transfer of Zn atoms due to Zn-O bonding, consistent with the XPS analysis. Figure 3e presents the Fourier transform of the Zn K-edge k3-weighted extended X-ray absorption fine structure (EXAFS) spectra, where the ZnO sample exhibited prominent peaks corresponding to Zn-O and Zn-Zn coordination. In contrast, the

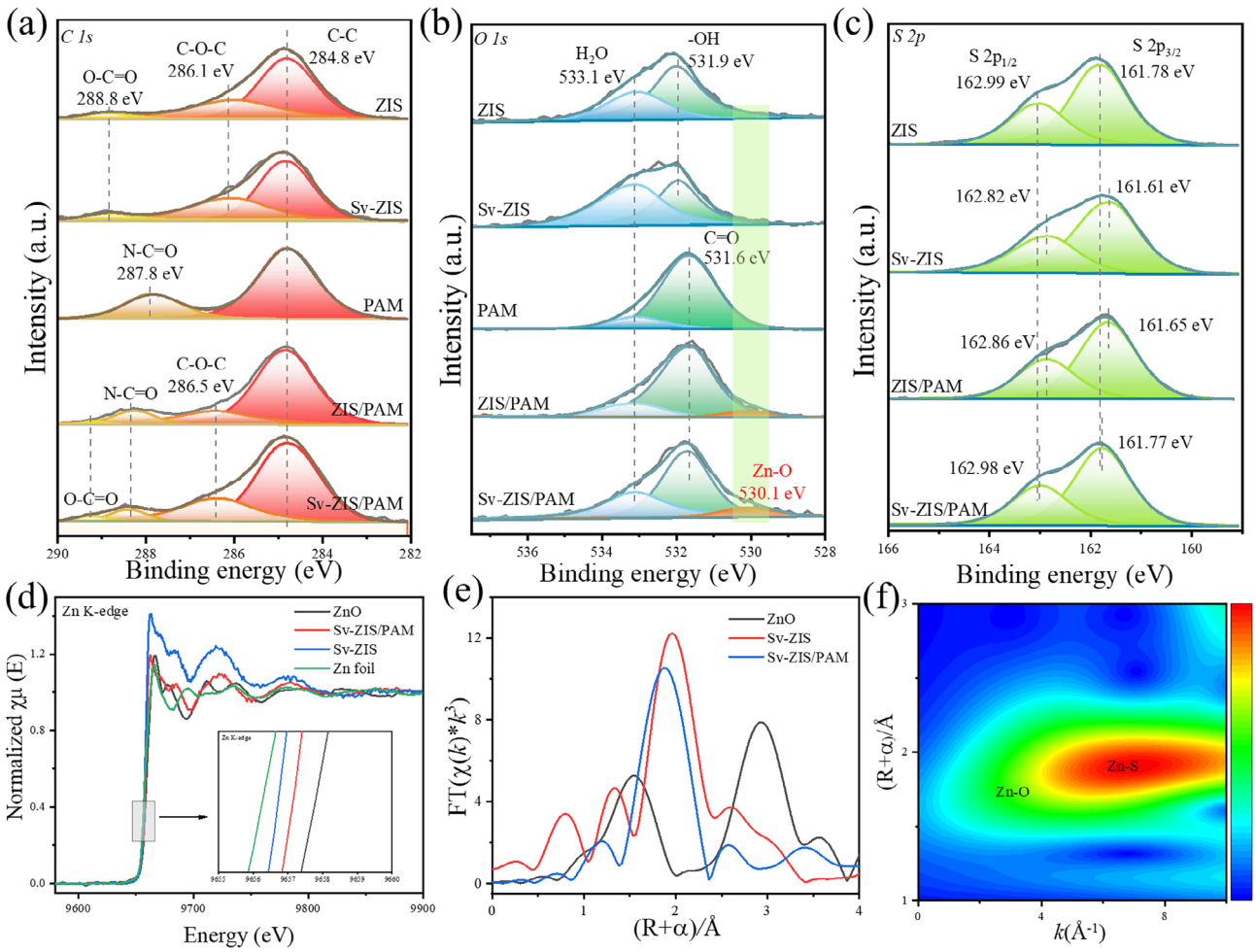

Figure 3. Chemical environment and coordination structure analysis of catalysts in hydrogel composites. XPS spectra of samples: a) C 1s, b) O 1s, c) S 2p. d) XANES spectra at Zn K-edge of samples, e) Fourier transform of the Zn K-edge EXAFS of samples, f) Wavelet transform plots of Zn K-edge in Sv-ZIS/PAM.

Sv-ZIS sample primarily showed a peak indicative of Zn-S bonding. The reduced intensity of the Zn-S peak in the Sv-ZIS/PAM samples may be because of the PAM matrix, which disturbs the coordination of Zn-S and alters its local structure. Figure 3e exhibited the Fourier-transformed (EXAFS) spectra signals recorded for samples. From the EXAFS fitting results in Table S2 (Supporting Information), the data confirmed the presence of Zn-O coordination in the Sv-ZIS/PAM sample. The low coordination number and the weak intensity of the Zn-O peak suggested that the Zn-O environment was more disordered than Zn-S bonding, corresponding to disordered vacancy sites. The weak Zn-O signal and low coordination number revealed that the Zn-O interaction in Sv-ZIS/PAM was more likely to be a coordination bond than a covalent bond. Furthermore, wavelet transform (WT) analysis was conducted to integrate the information from both R-space and k-space. The contour map of Sv-ZIS/PAM revealed features in k-space located at ≈3 and ≈7 $Å^{-1}$, corresponding to the Zn-O and Zn-S scattering paths, respectively, which aligns with the FT-EXAFS results.

To better understand the interaction between the catalyst and the hydrogel polymer chain, detailed computational and experimental analyses were conducted using density functional theory (DFT). **Figure** 4a schematically illustrates the interaction between ZIS/PAM and Sv-ZIS/PAM hydrogels. The influence of sulfur vacancies (Sv) on the charge distribution was first investigated. The removal of S atoms from the (001) crystal plane of ZIS facilitated the formation of stable Sv-ZIS structures.[41] The structural models of ZIS and Sv-ZIS are shown in Figure S13 (Supporting Information), which illustrates that ZIS has a nearly perfect hexagonal bilayer structure without any bond distortions (Figures S13a,b, Supporting Information), whereas the presence of Sv significantly alters the arrangement of neighboring atoms in the ZIS framework (Figure S13c,d, Supporting Information). Charge density distributions reveal that the positive charge density of Zn atoms near S vacancies is higher than that of other Zn atoms (Figure S14a, Supporting Information). This facilitated bonding between Zn atoms and N and O atoms of the polymer chains. The charge density difference indicated a significant charge redistribution in Sv-ZIS from Figure S14b (Supporting Information), alongside a distinct electron-depleted region detected at the sulfur vacancy sites. Zn atoms near the S vacancies transfer

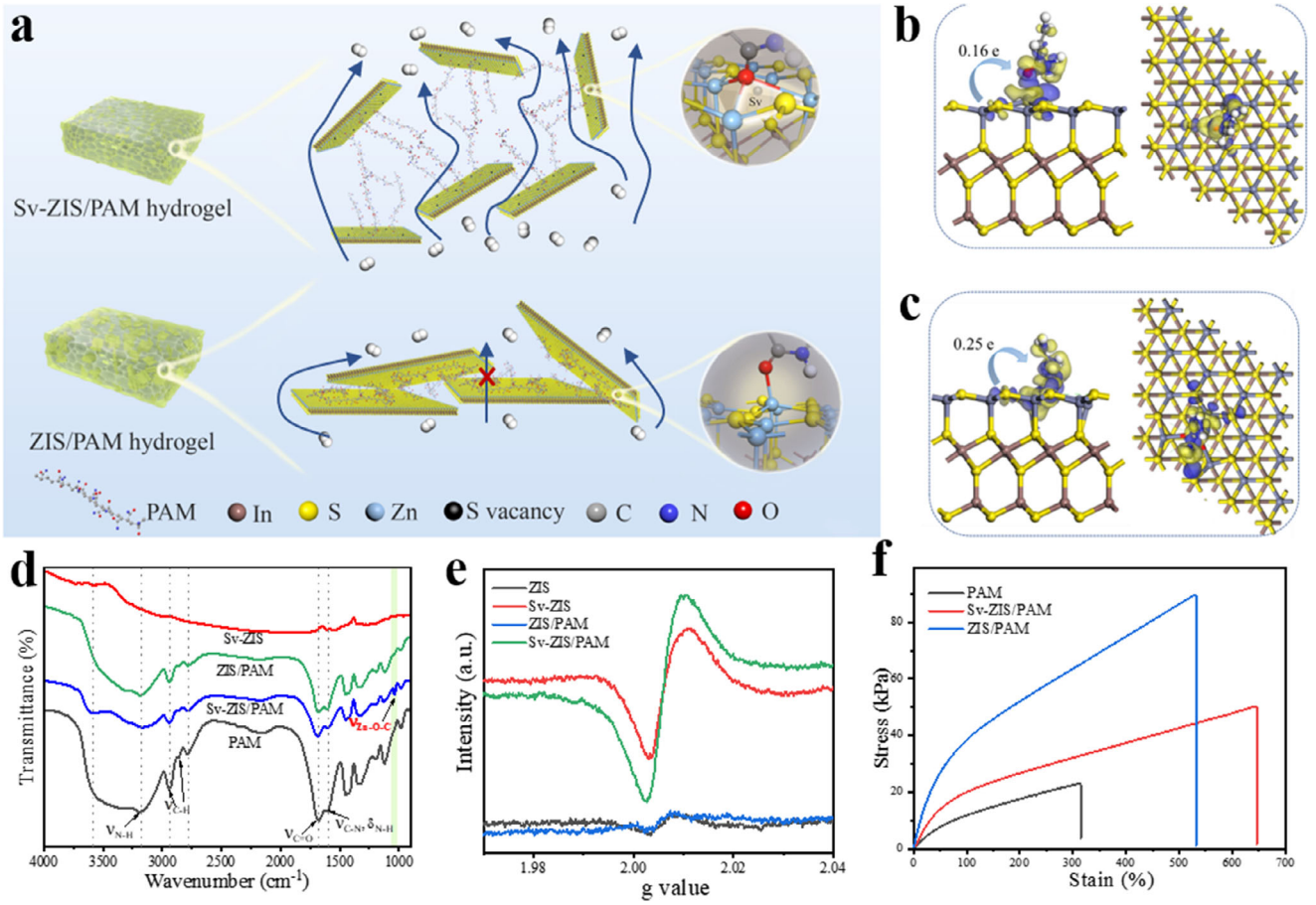

Figure 4. Integrated investigation of catalyst–polymer interactions and hydrogel performance. a) Schematic of polymer chains and catalyst interaction for ZIS/PAM and Sv-ZIS/PAM hydrogel. Electron density difference plots for b) ZIS and c) Sv-ZIS with adsorbed acrylamide (charge accumulation and depletion regions are represented in blue and yellow). d) FI-IR spectra, e) EPR spectra, and f) Strain-stress curves of samples.

electrons to adjacent sulfur atoms, consistent with XPS results. Additionally, the smaller size of Sv-ZIS nanosheets provides more pathways for mass transport when connected to polymer chains.

To further explore the specific binding modes between catalysts and acrylamide molecules during hydrogel formation, DFT was used to evaluate adsorption configurations and energies of acrylamide on ZIS and Sv-ZIS surfaces. Electrostatic potential and Mulliken charge analysis of acrylamide (Figure S15, Supporting Information) revealed potential adsorption sites. Structural models with multiple binding configurations (Figures S16 and S17, Supporting Information) show that both ZIS and Sv-ZIS preferentially form Zn-O and Zn-N bonds with acrylamide. The most stable configuration for both systems involves Zn–O coordination, consistent with XPS and XAS results. Notably, the adsorption energy of Sv-ZIS with acrylamide (−1.56 eV) is significantly lower than that of ZIS (−0.999 eV), indicating stronger interfacial binding in the Sv-ZIS/AM system. Therefore, the preferential adsorption at sulfur vacancies in Sv-ZIS ensured the adequate dispersion of AM on the catalyst surface, avoiding hindrance to photocatalytic active sites. Mulliken charge transfer analysis (Figure 4b,c) shows that acrylamide gains 0.25e from Sv-ZIS, compared to only 0.16e from ZIS, indicating stronger electronic coupling. Moreover, the polymer chains also plays a crucial role in modulating the electron distribution on photocatalyst surface, facilitating the desorption of H* adsorbed at the unsaturated sulfur sites after its reduction to hydrogen.[51]

DFT calculations confirmed the preferential formation of Zn-O bonds between the Zn atoms adjacent to sulfur vacancies and the oxygen atoms in acrylamide amide groups. This prediction was experimentally verified by FT-IR spectra (Figure 4d), where a new absorption peak at 1033 cm^{-1} in Sv-ZIS/PAM hydrogel is attributed to Zn-O-C bond formation.[52,53] This spectral feature directly supports the DFT-predicted coordination structure and highlights the specific chemical interaction between PAM and Sv-ZIS via Zn-O linkages.

The Zn-O coordination predicted by DFT was further supported by EPR measurements (Figure 4e). Compared with ZIS, Sv-ZIS exhibited a stronger EPR signal with a g value of 2.004 due to the presence of unpaired electrons at sulfur vacancy sites.[42] Notably, Sv-ZIS/PAM showed an even more pronounced signal, driven by the charge compensation effect of Zn-O bonding with oxygen in the amide groups.[54] This interaction redistributes charge and stabilizes unpaired electrons, amplifying the sulfur vacancy EPR signal. This experimental observation aligns with

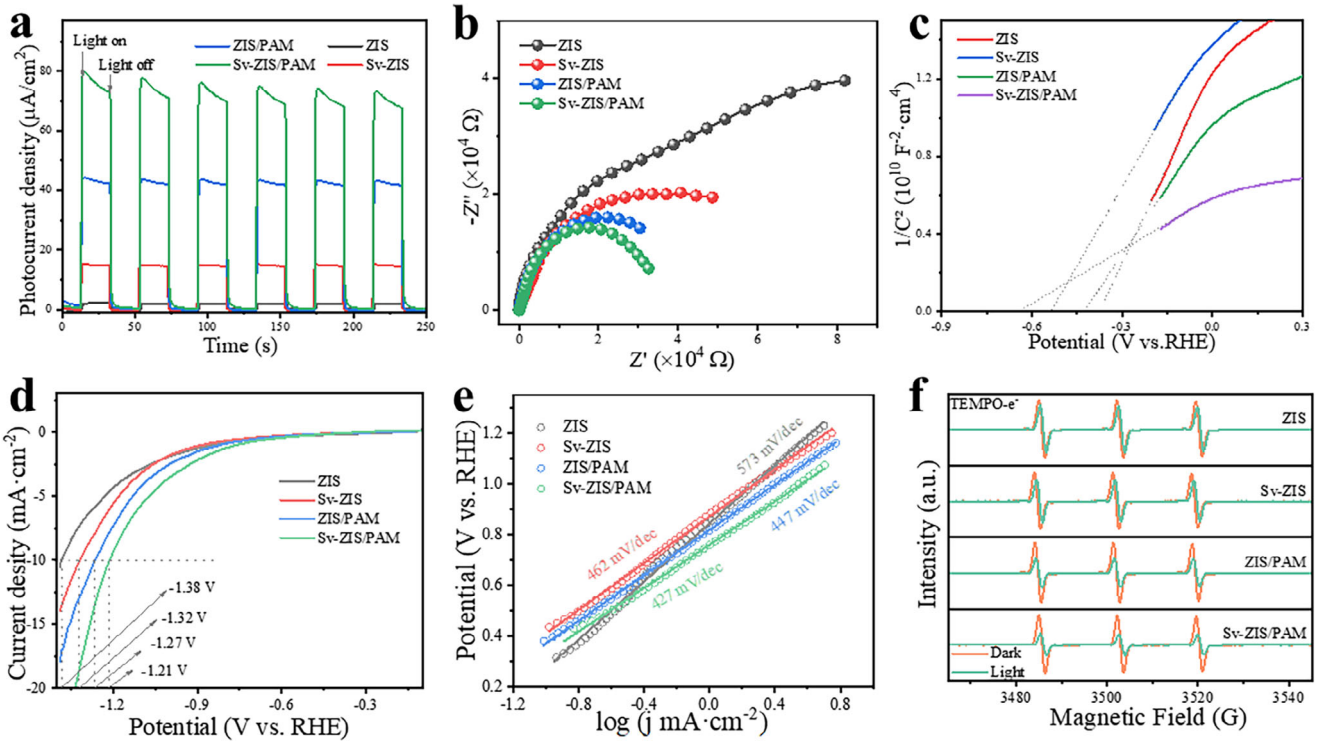

Figure 5. Photoelectrochemical and radical behavior characterization of hydrogel-based catalysts. a) Transient photocurrent response, b) EIS Nyquist plots, c) Mott–Schottky (M–S) plots at 1000Hz, d) LSV curves, e) Tafel slope plots, and f) EPR spectra of TEMPO-e$^-$.

the DFT-derived charge density maps showing electron depletion near Zn-O coordination zones.

As supported by FT-IR and EPR results, the amide groups in PAM can coordinate with Zn atoms in the catalyst, forming stable Zn-O bonds. To further clarify the role of Zn-O bonding in mechanical performance, DFT calculations (Figure S18, Supporting Information) show that the optimal adsorption site lies in the electron dissipation region around the Sv site. The optimized configurations reveal that Zn atoms adjacent to sulfur vacancies readily coordinate with oxygen atoms in the amide groups of PAM, forming triangular-pyramidal Zn-O bonding structures. This indicates dynamic coordination behavior under stress. DFT further reveals that the triangular-pyramidal Zn-O bonds formed near sulfur vacancies act as dynamic coordination cross-links within the hydrogel network. As shown in Figure 4f, the mechanical properties of PAM hydrogels with ZIS and Sv-ZIS photocatalysts were significantly improved. The ZIS/PAM hydrogel showed higher tensile strength, achieving a tensile stress of 89.7 kPa, with a tensile stress of 89.7 kPa, while the Sv-ZIS/PAM hydrogel showed superior ductility, with a maximum strain of 643.42%. Besides, the untreated PAM has a maximum tensile stress of only 23 kPa and the maximum tensile strain of only 312.8%. The significant increase in mechanical strength suggested a bonding interaction between the catalyst and the hydrogel polymer chains. The enhanced tensile strength of the ZIS/PAM hydrogel was also attributed to the aggregation of the catalyst during the polymerization process, leading to entanglement of the polymer chains around the catalyst, resulting in localized reinforcement of tensile strength. These multi-point Zn-O bonds act as dynamic coordination cross-links within the hydrogel network. The triangular-pyramidal structure enables local "slippage" or reorientation under external tensile force, effectively dissipating stress and delaying fracture. This mechanism explains the large increase in strain before breakage observed in the stress-strain curves of Sv-ZIS/PAM. Thus, the synergistic effect between sulfur vacancies and the amide groups not only enhances interfacial bonding strength, as supported by DFT, but also translates into improved flexibility and toughness at the macroscopic level. In addition, we have now performed cyclic tensile tests (Figure S19, Supporting Information) to assess the mechanical resilience of the Sv-ZIS/PAM composite. The hydrogel retains its structural integrity and exhibits excellent reversibility after repeated stretching cycles, further confirming that the introduction of sulfur vacancies improves not only the interfacial bonding but also the mechanical durability of the composite system.

2.2. Photoelectrochemical Properties

To elucidate the photoexcited charge separation and transfer, photoelectrochemical measurements were performed, to certify the critical role of the synergistic effect of acrylamide modification and sulfur vacancies in promoting the photocatalytic efficiency. As shown in **Figure 5**a, Sv-ZIS/PAM exhibited the highest photocurrent density than Sv-ZIS, ZIS, and ZIS/PAM, indicating the fast photogenerated carrier separation.[55] Impedance spectroscopy (EIS) was used to characterize the charge transfer resistance. A smaller arc radius corresponds to lower charge transfer resistance, indicating more efficient charge transfer, which

contributes to enhancing photocatalytic efficiency. The Sv-ZIS/PAM had the smallest radius arc observed in EIS, suggesting the lowest charge transfer barrier in Sv-ZIS/PAM (Figure 5b). The electrical equivalent circuit parameters for the sample's impedance data were listed in detail in Table S5 (Supporting Information). Mott–Schottky plots of ZIS, Sv-ZIS, ZIS/PAM, and Sv-ZIS/PAM at different frequencies were displayed in Figures S6a,b and S20a,b (Supporting Information). MS curves with positive slopes can be identified as n-type semiconductors. According to Equation S6 (Supporting Information), the carrier density of Sv-ZIS/PAM photocatalyst (3.35×10^{21} cm^{-3}) was higher than that of Sv-ZIS (1.13×10^{21} cm^{-3}), ZIS (8.95×10^{20} cm^{-3}) and ZIS/PAM (1.38×10^{21} cm^{-3}) from Figure 5c. The depletion width (W_d)of Sv-ZIS/PAM was calculated that decreased exactly from 4.48 to 3.06 nm as calculated by Equation S7 (Supporting Information). The results indicating Sv-ZIS/PAM accelerated the drift of the photo-excited carrier, effectively suppressing the recombination within the depletion region.[56]

The linear sweep voltammetry (LSV) curves (Figure 5d) reveal the electrocatalytic hydrogen evolution performance of the samples. Sv-ZIS/PAM exhibits the lowest onset potential (−1.21 V vs RHE), indicating superior catalytic activity. Correspondingly, the Tafel slope analysis (Figure 5e) shows that Sv-ZIS/PAM has the smallest slope (417 mV dec^{-1}), suggesting more favorable reaction kinetics and lower overpotential requirements. In general, a lower Tafel slope reflects faster hydrogen evolution kinetics.[57] These results highlight the enhanced HER activity due to the synergistic integration of Sv-ZIS with the polymer matrix. Based on the above results, the hydrogel-based photocatalyst shows enhanced photogenerated charge carrier separation efficiency, reduced separation difficulty, and increased carrier concentration compared to the pure photocatalyst. These improvements are attributed to the Zn-O bonding between ZIS and PAM, which is further strengthened by the presence of S vacancies in Sv-ZIS.

To further verify the influence of photogenerated electron behavior on photocatalytic activity, The electron signals of the prepared samples under dark and light conditions were analyzed by EPR using TEMPO as the trapping agent (Figure 5f).[58] All samples show the same TEMPO signal intensity under dark conditions, while the signal intensity of Sv-ZIS/PAM was significantly weakest compared to the other samples after 10 min illumination. This suggested that more photogenerated electrons in Sv-ZIS/PAM participate in reducing TEMPO to TEMPOH.[59] The results demonstrated that Sv-ZIS/PAM exhibits an enhanced ability to generate photogenerated electrons under illumination, followed by ZIS/PAM. Therefore, the synergistic effect of Zn-O bonding and S vacancies promotes the utilization of photogenerated electron transfer, which can effectively facilitate photocatalytic hydrogen production through water splitting.

2.3. Harnessing Atmospheric Moisture for Hydrogen Production Through Hygroscopic Hydrogel-Based Photocatalysis

Considering its hygroscopic and photocatalytic properties, the prepared samples was employed to assess photocatalytic hydrogen production in an atmospheric moisture environment. As can be seen in the hydrogen production performance splitting water vapor in **Figure 6a**, Sv-ZIS/PAM hydrogel exhibited the best photocatalytic hydrogen evolution performance in a water vapor environment, reaching 28.79 mmol/g_{cat}/h, which is ≈120 times the hydrogen evolution rate of ZIS powder (0.24 mmol/g_{cat}/h). Additionally, the isothermal water adsorption curves of PAM and Sv-ZIS/PAM at 25 °C (Figure 6b) show that the hydrogel maintains similar hygroscopic capacity after catalyst incorporation, further confirming its effectiveness in vapor-phase hydrogen production. The apparent quantum efficiency (AQE) of Sv-ZIS/PAM was estimated using different band-pass filters, showing a high AQE of 35.1% at 365 nm (Figure 6c), correlating well with its UV–vis absorption spectrum, indicating predominant H_2 generation via photocatalysis. This enhancement is attributed to the combined effects of the hydrogel network, hygroscopicity, and interaction between the polymer chain and the catalyst in the Sv-ZIS/PAM system. As a comparison, the physical mixture of Sv-ZIS and hydrogel shows a hydrogen evolution rate nearly identical to that of pure Sv-ZIS, as presented in Figure S21a (Supporting Information). The slight increase observed can be attributed to the hydrogel's passive water-retention ability, which helps maintain surface moisture but lacks the interfacial bonding and charge modulation present in the integrated composite.

To obtain a more comprehensive understanding of HER, the Gibbs free energy change (ΔG_{H^*}) for H* adsorption over the surface of ZIS, Sv-ZIS, ZIS/AM and Sv-ZIS/AM was assessed in Figure 6d. Hydrogen adsorption approaches zero energy, indicating low barriers for both adsorption and desorption.[60] The free energy of hydrogen adsorption for Sv-ZIS/AM is found to be 0.02 eV, indicating significantly more favorable H_2 evolution activity compared to ZIS (−1.09 eV), Sv-ZIS (−0.58 eV), and ZIS/AM (−0.35 eV). This result is consistent with the reaction kinetics revealed by electrochemical measurements, including Tafel slope analysis and electrochemical impedance spectroscopy (EIS). Sulfur vacancies modulate the electron distribution of ZIS, thereby lowering the reaction energy barriers for H* adsorption on S and H_2 desorption. Polymeric chain molecules play a similar role in regulating the electron distribution of ZIS. This suggests that the synergistic effect of acrylamide modification and sulfur vacancies can effectively modulate the electronic structure of ZIS and optimize the Gibbs free energy of the HER reaction, leading to excellent photocatalytic H_2 evolution activity.

Notably, the network regulation effect of Sv-ZIS/PAM hydrogel was more pronounced in a water vapor environment (28.79 mmol/g_{cat}/h) compared to liquid water (10.636 mmol/g_{cat}/h), exhibiting a 2.71-fold increase. The main reason is that the integration of the photocatalyst with the hydrogel enhances the catalyst's water molecule adsorption capacity, as the efficiency of the water decomposition depends on the amount of adsorbed water molecule layers, thereby boosting hydrogen production performance.

Furthermore, modulating the crosslinker content was the easiest way to adjust the hydrogel network structure, thereby controlling the adsorption of water molecules by catalysts on the polymer chains. In moisture environment, modulating the hydrogel network had a significant enhancement on the hydrogen production performance of the catalyst. The hydrogen production performance initially increased and then decreased with the rising crosslinking agent concentration, reaching its peak at an addition amount of 0.0045 g, with a hydrogen production rate of 28.79 mmol/g_{cat}/h (Figure S22, Supporting Information). As a

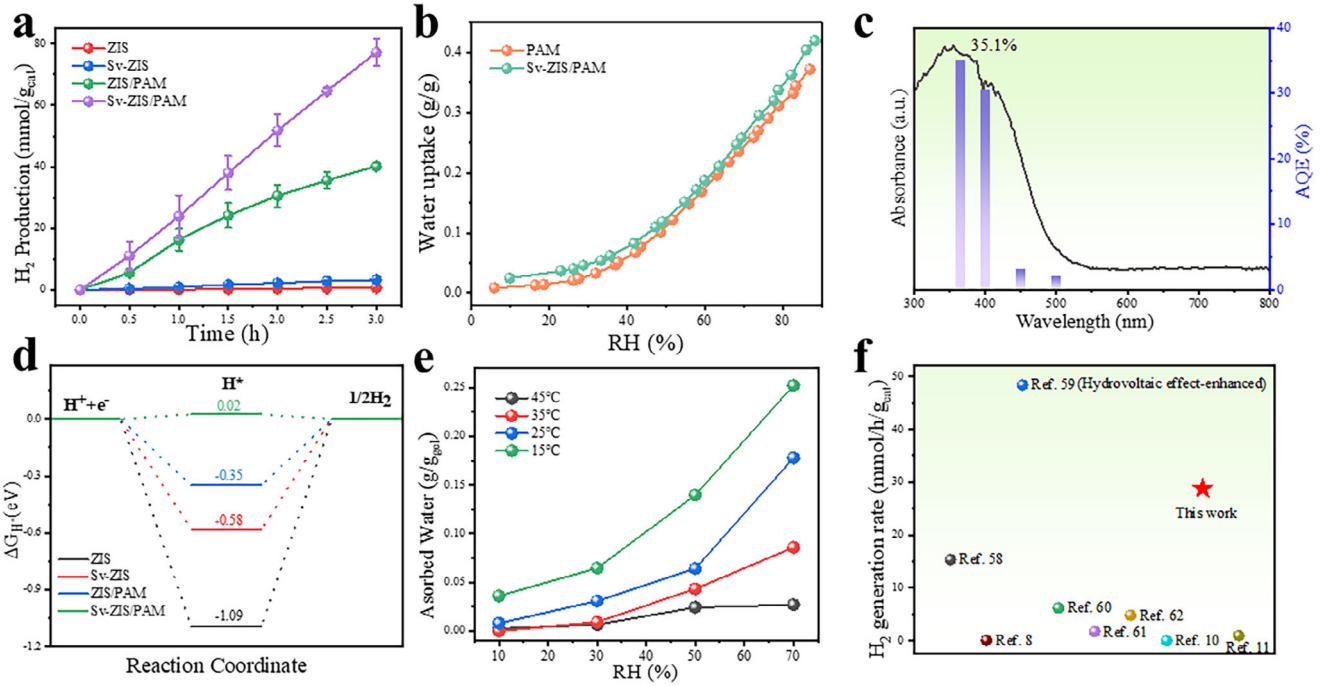

Figure 6. Hydrogen production from harvesting moisture via hygroscopic hydrogel-based photocatalysis under 100 mW cm^{-2} illumination. a) The comparison of photocatalytic water vapor splitting performance of samples. b) Water adsorption isotherm of PAM and Sv-ZIS/PAM at 25 °C. c) Wavelength dependence of the apparent quantum efficiency (AQE) for Sv-ZIS/PAM. d) ΔG_{H*} for HER over the surface of ZIS, Sv-ZIS, ZIS/AM, and Sv-ZIS/AM. e) Water absorption isotherms of the Sv-ZIS/PAM with a crosslinker amount of 0.0045g at 15, 25, 35, and 45 °C during 3 h. f) The comparison of reference studies on photocatalytic water vapor splitting performance.

control, we tested the hydrogen production of Sv-ZIS/PAM hydrogels in water with various crosslinker content. The results showed that the crosslinker concentration had minimal effect on hydrogen production in water (Figure S23, Supporting Information), which can be attributed to the limited effect of adjusting the hydrogel's network structure on the water layers adhering to the catalysts on the polymer chains in water. Additionally, the thickness of the hydrogel affects the transfer of moisture within the gel after hygroscopicity and the diffusion of hydrogen gas production. Excessive thickness can impede hydrogen gas diffusion, while being too thin results in pronounced dehydration under illumination. Through testing, we determined the optimal thickness to be 2 mm (Figure S24, Supporting Information).

The effects of reaction temperature and humidity conditions were also investigated. The temperature and humidity in the reactor reached 30 °C and 44.6% RH quickly within 30 min of illumination (Figure S25, Supporting Information), and slow growth (T: 30+3.9 °C, RH: 44.6 + 7.4%) for the 3 h reaction under illumination, which was enough for Sv-ZIS/PAM to collect water from the reactor according to the water adsorption curve. As shown in Figure 6e, at low humidity (lower than 30%), the absorbed water was less than 0.1 g/g_{gel}. However, as the RH is increased above 50%, the saturated water uptake increases significantly. The increase in temperature enhanced the thermal motion of water molecules and accelerated the desorption of water molecules from the hydrogel, thereby reducing the water content within the hydrogel. Compared to recent photocatalytic hydrogen production systems that utilize water vapor or moisture, this work demonstrates significantly better hydrogen production performance than most systems (Figure 6f).[8,11,12,61–65]

Furthermore, the synthesis method of the hydrogel, the catalyst loading, and the photocatalytic performance in liquid water were also investigated. In hydrogel synthesis methods, redox initiation demonstrated superior efficacy in polymerization initiation, followed by thermal initiation, with photoinitiation exhibiting the least effectiveness owing to radical occupancy of active sites (Figure S26, Supporting Information). The prepared powder photocatalysts and hydrogel photocatalysts were tested for photocatalytic hydrogen production in water. Sv-ZIS nanosheets showed the higher H_2 generation efficiency (2.190 $mmol/g_{cat}/h$), which was significantly better than that of ZIS (1.089 $mmol/g_{cat}/h$) (Figure S27a, Supporting Information). The improved performance of Sv-ZIS can be attributed to the capture of photogenerated charge by the S vacancy and the modulation of the electronic structure. The Sv-ZIS/PAM hydrogels displayed a noteworthy H_2 evolution rate (10.636 $mmol/g_{cat}/h$), marking a 2.24-fold increase compared to ZIS/PAM (4.739 $mmol/g_{cat}/h$). Optimal catalyst loading enables maximal utilization of interaction with the polymer chains. Excessive loading, however, results in an abundance of binding sites, leading to polymer chain shortening and catalyst stacking (Figure S27b, Supporting Information). In addition, Sv-ZIS/PAM exhibited excellent stability after more than 30 h (Figure S27c, Supporting Information), suggesting its potential for sustained photocatalytic performance.

To expand the application for simultaneous indoor humidity control and hydrogen production, the sealed reactor was tested with LED light instead of solar illumination. The temperature,

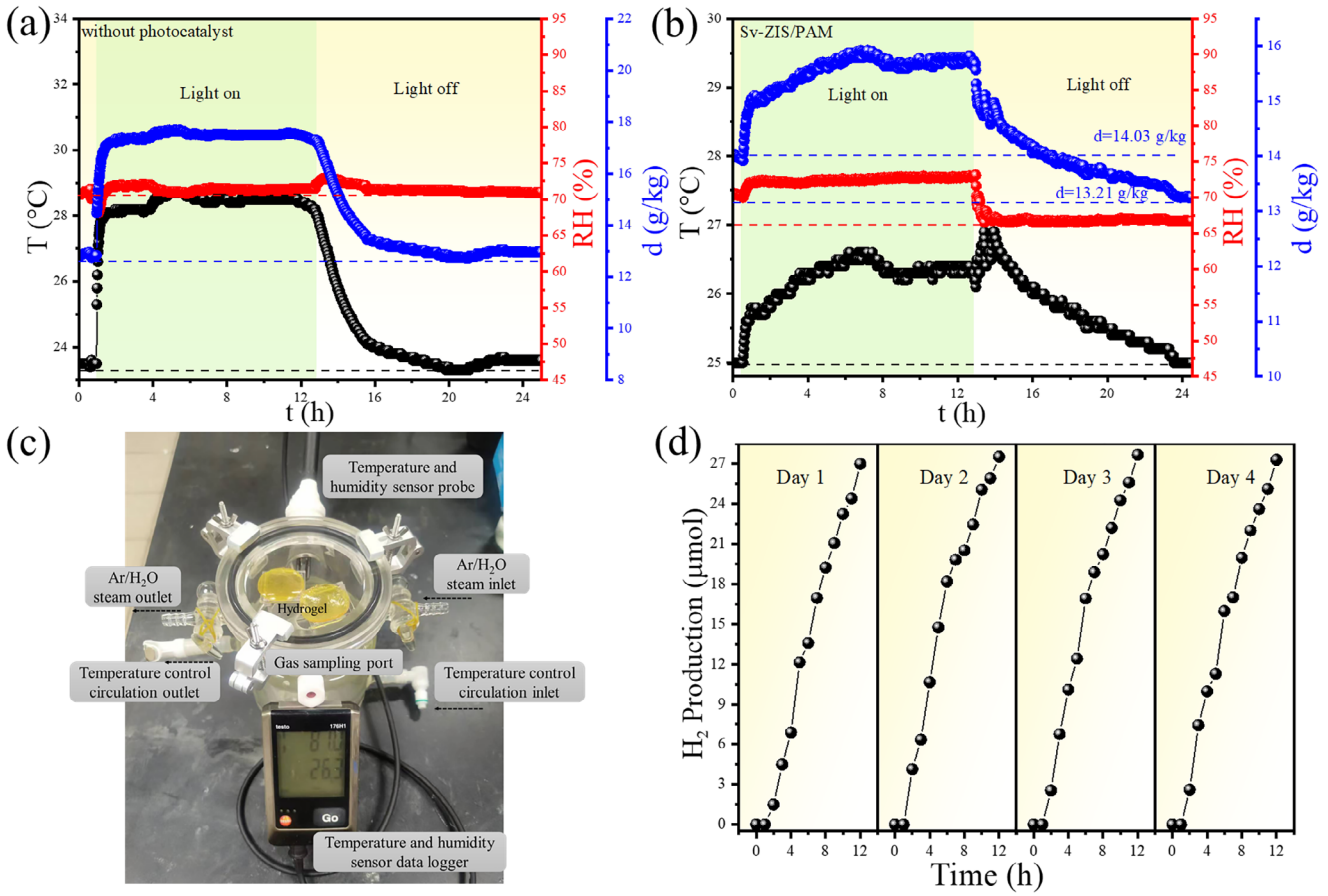

Figure 7. Dehumidification properties. The temperature, relative humidity, and moisture content changes by placing the PAM hydrogel a) and Sv-ZIS/PAM hydrogel b) into the seal reactor with an initial relative humidity of 75% for 24h, including 12 h LED light illumination; c) The photograph of photocatalytic water vapor splitting and dehumidification system. d) The hydrogen generated through the photocatalytic dehumidification cycle operation of Sv-ZIS/PAM.

relative humidity, and moisture content changes by placing two hydrogel pieces (≈2 g) of the PAM hydrogel (**Figure** 7a) or Sv-ZIS/PAM hydrogel (Figure 7b) into a 0.5 L seal reactor with an initial relative humidity of 75% for 24h. The LED lamp emits light in the visible spectrum range of 400–750nm, resulting in minimal heat generation. The relative humidity and moisture content of the PAM hydrogel without photocatalyst were almost unchanged at the same temperature before and after light exposure (Figure 7a), while the relative humidity of the Sv-ZIS/PAM sample decreased from 70.6 to 66.7% and the moisture content decreased from 14.03 to 13.21 g kg^{-1} (Figure 7b). And hydrogen production reached 27 μmol after 12 h of LED light illumination, matching the amount of consumed moisture in Figure 7c. Cyclic testing over 4 days revealed no significant performance decreased in Figure 7d, which signifies its exceptional performance even under low light power density. When compared to the hydrogel without photocatalyst, the hydrogel with photocatalyst exhibits a lesser increase in ambient temperature and a greater increase in humidity. This can be attributed to the ability of the Sv-ZIS catalyst to absorb visible light, facilitating evaporation of water absorbed by the hydrogel resulting in environmental cooling. This also suggested its potential for indoor dehumidification applications. The XPS spectra (Figure S28, Supporting Information) reveal no significant change in the chemical states of Zn, In, S, O, and C after cycling, confirming that the electronic environment of key elements remains stable. Meanwhile, the SEM images and EDS mapping (Figure S29, Supporting Information) demonstrate that the porous hydrogel structure and nanosheet morphology are well preserved, with no obvious aggregation or collapse. The uniform elemental distribution also supports that the catalyst remains evenly dispersed in the matrix. These results together verify that the Sv-ZIS/PAM maintains both chemical and morphological stability after repeated photocatalytic cycles, supporting its long-term durability.

2.4. Molecular Dynamics Investigation of the Impact of Adsorbed Moisture Distribution on Water Splitting

The hydrogel is a 3D network composed of polymeric chains. The moisture adsorbed in hydrogels was categorized into three states based on its distance from the polymer chain: free water (FW), intermediate water (IW), and bound water (BW). To determine which type of water in the hydrogel decomposes preferentially, a molecular dynamics (MD) simulation was performed to compare the interaction energies of water with the hydrogel

polymer chains. The results showed water molecules in the IW layer were more readily decomposed, and the decomposition difficulty of individual water molecules in the FW and IW layers remained similar across different degrees of cross-linking. This was investigated by first constructing simulation models where water molecules were unevenly distributed in the pores formed by the polymer chains (snapshots of the model are shown in Figure S30a–c, Supporting Information). We then calculated the total and average interaction energies between water molecules in each layer and the polymer chains under varying cross-linker concentrations (Figure S30d,e, Supporting Information). Additionally, Figure S31 (Supporting Information) shows hydrogel models with different cross-linker contents but the same water content. The average interaction between a single water molecule in the IW layer and the polymer chains was slightly larger than that in FW layer, while the average interaction between a single water molecule and the polymer chains was notably higher in the BW layer than that in IW and FW. The slight difference in interaction energy between IW and FW under various cross-linking degree implies similar decomposition challenges for a single water molecule in both layers. Consequently, water molecules in the IW layer experience interactions from both adjacent layers. This intermediate positioning likely places the IW water molecules in a relatively active state, thereby facilitating their decomposition.[66]

To gain molecular-level insights into how the pyramidal Zn–O structure regulates water distribution in hydrogels and enhances catalytic activity, we conducted molecular dynamics (MD) simulations. The results revealed the pyramidal structure of Sv-ZIS enhances water retention and bonding with polymer chains, significantly influencing polymer chain extension and water distribution within the hydrogel. Using a hydrogel model with 10% water content under 0.0045 g crosslinker (**Figure** 8a–c), the RDF curves (Figure 8d,e) further support this observation: Sv-ZIS/PAM exhibits stronger polymer–water interactions, particularly at short distances, suggesting a more optimized water network structure. The coordination number (CN) analysis shows that water molecules near N and O atoms in PAM have an average coordination number close to 1 at short distances, corresponding to tightly bound water in the first hydration shell. In contrast, at longer distances associated with IW and FW, the coordination number increases to ≈2.5–4, indicating that water in these regions is less structured and less likely to form full fourfold coordination, consistent with intermediate water. This confirms the accuracy of the water-state segmentation and highlights that the Zn-O pyramidal coordination enhances the proportion of such catalytically relevant IW. The radius of gyration (Rg) values were also larger for Sv-ZIS/PAM (Figure 8f), indicating that the polymer chain extension in Sv-ZIS/PAM was superior to that in ZIS/PAM and PAM. Further MD simulations at higher water content (50%) (Figure S32, Supporting Information) revealed consistent trends. In the ZIS/PAM, polymer chains interact directly with Zn atoms on the ZIS catalyst without specific binding sites, allowing the chains to extend over the surface. However, the pyramid structure formed by Zn atoms near sulfur vacancies facilitated stronger interactions with polymer chains, resulting in more extensive chain extension. Figure 8g provides a schematic illustration of the water molecule distribution near the catalyst interface, showing that intermediate water (IW) is most likely to reside closest to the active sites on the catalyst. This spatial configuration is key to its reactivity.

To unravel the underlying mechanism by which the catalyst affects the water state distribution within the hydrogel, low-field nuclear magnetic resonance (LF-NMR) and differential scanning calorimetry (DSC) were employed to analyze PAM, ZIS/PAM, and Sv-ZIS/PAM systems. The goal was to determine how the introduction of Zn-O coordination bonds between the catalyst and PAM influences the formation and confinement of IW. As shown in Figure 8h, the T_2 relaxation profiles obtained from LF-NMR clearly distinguish three types of wate.[67–69] In PAM hydrogel, FW dominates, while BW and IW are present in smaller proportions, indicating relatively weak confinement of water molecules by the polymer matrix. Upon incorporation of ZIS (without sulfur vacancies), IW content increases modestly due to physical adsorption of water on the catalyst surface. However, due to the abundance of surface adsorption sites and the tendency of ZIS with PAM chains to aggregate, the interfacial structure lacks uniformity, limiting further transformation of water into IW.

In contrast, the Sv-ZIS/PAM composite exhibits a significantly higher proportion of IW and a corresponding reduction in FW, while BW remains nearly unchanged. This shift in water state distribution can be attributed to the formation of Zn-O coordination bonds between the PAM chains and the Zn atoms exposed at sulfur vacancy sites. This coordination interaction strengthens the interface between the polymer and catalyst, creating a confined environment that effectively regulates water molecule dynamics. As a result, more water molecules adopt an intermediate state—loosely associated with the matrix, dynamically responsive, and more reactive in interfacial photocatalytic processes. This interpretation is strongly supported by DSC analysis (Figure S33, Supporting Information). The pure PAM shows a sharp endothermic melting peak near 0 °C with relatively high enthalpy, corresponding to the presence of abundant freezable FW.[70,71] In ZIS/PAM, the melting peak slightly shifts toward lower temperatures, indicating a partial transition of FW into weakly bound water. However, Sv-ZIS/PAM exhibits a broadened and further downshifted melting peak with much lower enthalpy, suggesting that a substantial portion of water exists in non-freezable or intermediate forms. This behavior indicates stronger interactions between water and the composite network, due to both the polymer and the coordinated catalyst surface.

In summary, the introduction of Zn-O coordination not only improves catalyst dispersion and inhibits aggregation but also leads to a favorable redistribution of water molecules, increasing the proportion of IW. This creates a dynamic water environment conducive to efficient interfacial charge transport and reaction kinetics in atmospheric water harvesting and photocatalysis applications.

3. Conclusion

This study proposes a novel strategy for green hydrogen production directly from ambient humidity by engineering a triangular-pyramid Zn-O bonding configuration between PAM hydrogel and Sv-ZIS nanosheets. The innovative structure harnesses the synergistic properties of polymer matrices and sulfur vacancy-rich catalysts. By tailoring the polymer-catalyst interface, the design achieves enhanced charge dynamics, efficient reactant

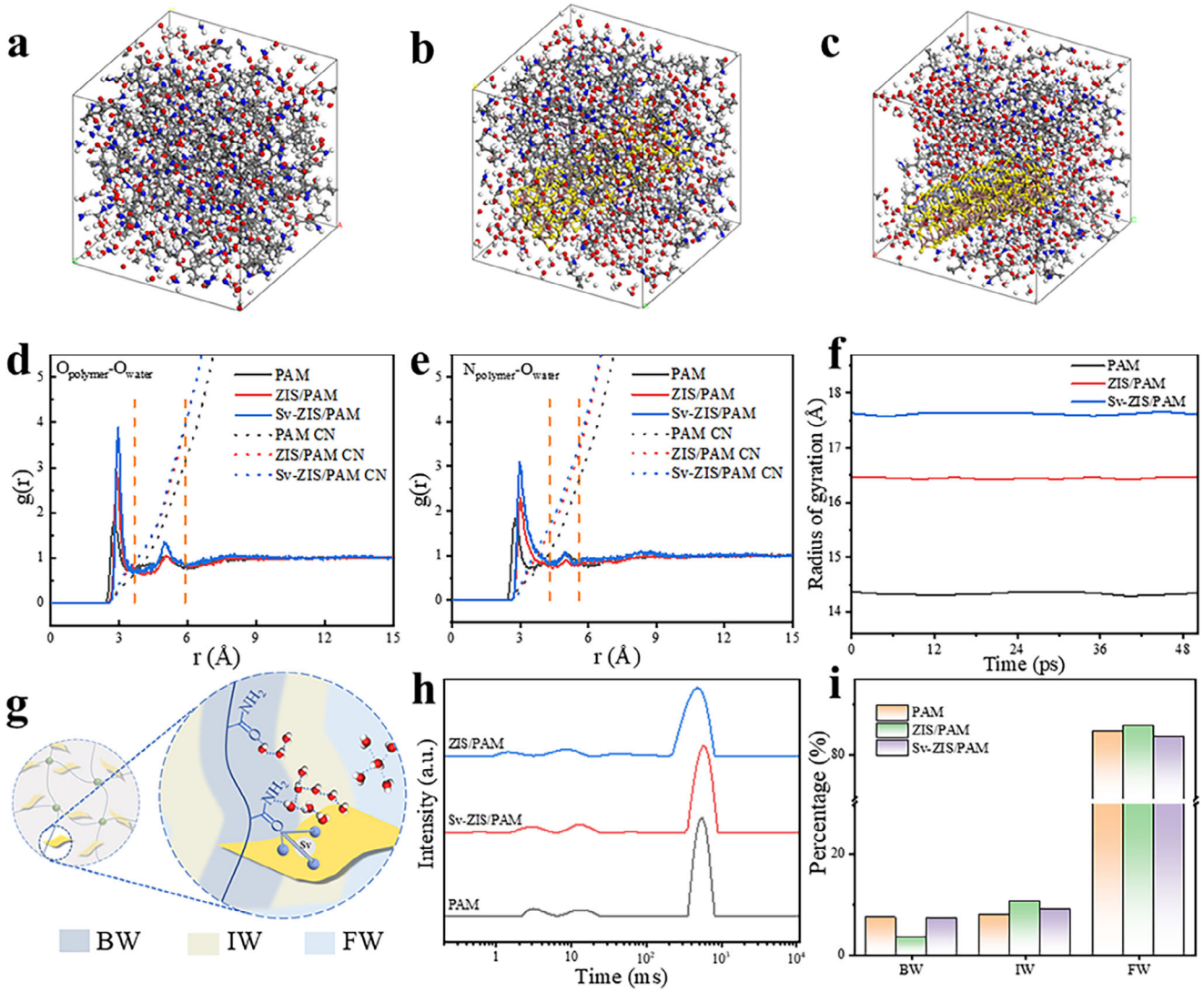

Figure 8. Comprehensive analysis of hydrogel–photocatalyst interactions. The trajectory snapshot of different photocatalyst in the hydrogel model containing 10% water content under 0.0045 g crosslinker: a) PAM, b)ZIS/PAM, c) Sv-ZIS/PAM. d) RDF: $O_{polymer}$−O_{water}; e) RDF: $N_{polymer}$−O_{water}; f) Radius of Gyration (R_g) of Polyacrylamide Hydrogels containing different photocatalysts as a function of simulation time. g) Schematic illustrating that intermediate water (IW) is preferentially distributed near the catalyst within the hydrogel network. h) The relaxation time spectrum of LF-NMR and i) the proportion of the three water (BW, IW, FW) based on the corresponding peak areas.

and product transport, and stable hydrogen evolution performance under diverse outdoor and indoor conditions, overcoming the limitations in conventional water-based photocatalytic systems.

DFT and Molecular dynamics simulations, along with characterizations, reveal that the triangular-pyramid configuration optimizes moisture adsorption and utilization and reduces hydrogen desorption energy to 0.02 eV, thereby significantly improving hydrogen evolution reaction (HER) activity. This engineered structure increases water binding sites, promotes polymer chain extension, and improves the ratio of bound to intermediate water molecules, facilitating efficient moisture-to-hydrogen conversion. Additionally, this structure reinforces the hydrogel's tensile strength and system stability, ensuring durability in long-term applications.

Under ambient conditions (≈30 °C, 50% RH) with 100 mW cm^{-2} irradiance, the system achieves a hydrogen evolution rate of 28.79 mmol/gcat/h, accompanied by an apparent quantum efficiency of 35.1% at 365 nm. Under low-intensity LED illumination (≈10 mW cm^{-2}), the system demonstrates effective dehumidification capabilities, reducing humidity by 0.82 g kg^{-1} in a closed reactor, further highlighting its suitability for indoor applications. Moreover, the scalable, mild in situ polymerization process ensures compatibility with industrial-scale production, paving the way for broad practical implementations.

This study highlights the promising potential of polymer-catalyst bonding structures in exploiting atmospheric humidity for hydrogen production. By addressing critical challenges in moisture adsorption, charge separation, and catalytic activity, it provides a reliable framework for advancing humidity-driven

hydrogen production technologies and contributes to the development of practical sustainable energy solutions.

4. Experimental Section

Materials: $InCl_3{\cdot}4H_2O$, thioacetamide, Acrylamide, *N,N′*-methylenebis(acrylamide) and N,N-tetramethylenediamine were purchased from Shanghai Macklin Co., Ltd. $H_2PtCl_6{\cdot}6H_2O$ was purchased from Sinopharm Chemical Reagent Co., Ltd. $Zn(CH_3COO)_2{\cdot}_2H_2O$, potassium persulfate and triethanolamine were purchased from Shanghai Runjie Chemical Reagent Co., Ltd. All chemicals were used as received without further treatment.

Fabrication of Sv-ZIS Photocatalysts: $Zn(CH_3COO)_2{\cdot}_2H_2O$ (1.5 mmol) and $InCl_3{\cdot}4H_2O$ (3 mmol) was dissolved in 250 mL deionized water. Then, 8 and 6 mmol thioacetamide was added into the above solution after vigorous stirring 30 min to synthesis Sv-ZIS and ZIS, respectively. Next, the mixed solution was maintained stirring at 95 °C for 5 h. The pre-samples were obtained by collecting the solid by centrifugation followed by washing with deionized water for twice. After that, the obtained samples were dispersed into deionized water with sonication for each 30 min, and subsequently large aggregates were removed by centrifugation for 5 min at 6000 rpm until the upper liquid becomes clear. Finally, the colloidal nanosheets were obtained, and the concentration of nanosheets was ca.1 mg mL^{-1}. To verify the exact solid content in solution, 50 mL of solution was taken and freeze-dried, and the solid sample obtained was weighed and calculated.

Fabrication of PAM, ZIS/PAM, and Sv-ZIS/PAM Hydrogels: PAM, ZIS/PAM, and Sv-ZIS/PAM hydrogels were prepared by the radical polymerization. The prepared photocatalyst underwent a polymerization reaction with monomers, initiated by various methods including thermal initiation, photo initiation, and redox initiation. Since no specific initiation method was mentioned in the text, it indicates that the gel preparation proceeded via redox initiation. When photoinitiated, no crosslinker needs to be added, and the polymerization process was carried out using LED light for 5 h. The photocatalytic nanosheets can serve as both crosslinkers and photoinitiators.[72] When thermally initiated, no accelerators needs to be added, and the polymerization was conducted at 70 °C for 5 h. The monomer acrylamide (AM, 0.5 g) were dissolved in water (5-*x* mL), Sv-ZIS nanosheets suspension was then added (*x* mL). The crosslinker *N,N′*-methylenebis(acrylamide) (BIS, 0.0045 g), potassium persulfate (KPS, 0.005 g) and 20 µL N,N-tetramethylenediamine (TEMED) were subsequently added into the above suspension. The polymerization was performed at 25 °C for 12 h in dark. Finally, the hydrogel washed with deionized water to remove the unreacted monomers, cross-linker and initiator. The obtained sample was referred to as Sv-ZIS/PAM. The catalyst obtained by adding different amounts of Sv-ZIS suspension was denoted as *x*-Sv-ZIS/PAM. The sample Sv-ZIS/PAM marked in this work indicated that the added amount was 3 mL. And the ZIS/PAM hydrogel was prepared similarly to the above procedure. The preparation of PAM hydrogel was similar to the procedure described above, except that AM was dissolved in water (5 mL).

Photocatalytic H_2 Production: Photocatalytic H_2 production reaction was carried out in an automatic online trace gas analysis system (Labsolar 6A, Beijing Perfectlight Technology Co., Ltd) connected to a gas chromatograph instrument (GC9790II, Fuli, TCD with Ar as the carrier gas, 5 Å molecular sieve column) and kept at 5 °C, 5.3 kPa during the reaction. The light source was a 300 W Xenon arc lamp (PLS-SXE300D, AM 1.5G, 100 mW cm^{-2}, Beijing Perfectlight Technology Co., Ltd) equipped with liquid infra-red filter to remove large amounts of heat. The intensity of the light was measured by a full-spectrum strong light optical power meter (OHSP-350 UV, Hopoocolor, China). The corresponding Xenon lamp spectra is shown in Figure S34a (Supporting Information). Measurements of the powder were performed in water, while those of hydrogel-supported ZIS were performed in water. For the measurements of the powder, 50 mg photocatalyst was dispersed in 100 mL aqueous solution containing 10 mL triethanolamine (TEOA) and $H_2PtCl_6{\cdot}6H_2O$ (165 µL, 4 g L^{-1}, Pt corresponding to 0.5% of the mass of photocatalyst) with a continuous stirring process. Gas chromatography was employed to determine the amount of produced H_2. Cycling photocatalytic tests were conducted using the same procedure after collecting and washing the samples with water. Photograph of the automatic online trace gas analysis system was displayed in Figure S35 (Supporting Information).

Due to its hygroscopic and photocatalytic properties, the hybrid Sv-ZIS/PAM hydrogel was utilized for evaluating photocatalytic hydrogen production in a water vapor environment. The Sv-ZIS/PAM hydrogel, having undergone the photodeposition Pt process, was cleaned, dried, and positioned on the sand core glass triangle shelf ≈6 cm above the reactor's bottom. Subsequently, 50 mL of water was introduced into the reactor as a humid air environment for photoreaction process. The reactor was connected to a circulating cooling water system to keep at 25 °C during the reaction. Gas chromatography was employed to determine the amount of produced H_2.

Synchronous Hydrogen Production and Dehumidification Experiments for Indoor Environment: The hybrid Sv-ZIS/PAM hydrogel used was identical to that employed in the water vapor hydrogen production, with the exception that two hydrogel pieces were placed in a sealed 500 mL container under initial conditions (T: ≈24°C, ≈70%). As a control, a gel without the addition of a catalyst underwent the same testing procedures. Before introducing the hydrogel into the sealed reactor, it underwent exposure to atmospheric conditions for water absorption until saturation was achieved. This step was crucial in ensuring that the observed changes in humidity within the tube were not attributed to any additional capture by the hydrogel. The LED daylight (30 W, 2400 lux, 10 mW cm^{-2}) as the indoor light source and the corresponding spectra was displayed in Figure S34b (Supporting Information). And Ar was blown into the water to adjust the humidity and remove the air. Temperature and humidity sensor were used to record the changes of temperature and humidity in the reactor, and the produced gas was injected into the gas chromatograph with gas syringe for gas analysis.

Characterizations, Molecular Dynamics Simulation, and DFT Calculations: The details can be found in the Supporting Information.

Supporting Information

Supporting Information is available from the Wiley Online Library or from the author.

Conflict of Interest

The authors declare no conflict of interest.

Data Availability Statement

The data that support the findings of this study are available from the corresponding author upon reasonable request.

Keywords

DFT simulation, humidity-to-hydrogen, hydrogel-based photocatalysis, polymer-catalyst bond, sulfur vacancies

Received: June 22, 2025
Published online:

[1] L. Lei, W. Wang, C. Wang, H. Fan, A. K. Yadav, N. Hu, Q. Zhong, P. Müller-Buschbaum, *J. Mater. Chem. A* **2020**, *8*, 23812.
[2] T. Nishino, M. Saruyama, Z. Li, Y. Nagatsuma, M. Nakabayashi, N. Shibata, T. Yamada, R. Takahata, S. Yamazoe, T. Hisatomi, K. Domen, T. Teranishi, *Chem. Sci.* **2020**, *11*, 6862.
[3] Y. Liu, H. Duan, *Fundam. Res.* **2024**, *5*, 913.
[4] T. Suguro, F. Kishimoto, K. Takanabe, *Energy Fuels* **2022**, *36*, 8978.

[5] G. Li, K. Zhou, Q. Sun, W. Ma, X. Liu, X. Zhang, L. Zhang, B. Rao, Y.-L. He, G. He, *Angew. Chem., Int. Ed.* **2022**, *61*, 202115298.
[6] X.-W. Zhang, F. Wang, C.-C. Wang, P. Wang, H. Fu, C. Zhao, *Chem. Eng. J.* **2021**, *426*, 131927.
[7] Z. Liu, T. Yi, C. Huang, K.-L. Choy, C. Liu, *Energy AI* **2021**, *6*, 100102.
[8] Y. Liu, W.-K. Han, W. Chi, J.-X. Fu, Y. Mao, X. Yan, J.-X. Shao, Y. Jiang, Z.-G. Gu, *Appl. Catal., B* **2023**, *338*, 123074.
[9] T. Suguro, F. Kishimoto, N. Kariya, T. Fukui, M. Nakabayashi, N. Shibata, T. Takata, K. Domen, K. Takanabe, *Nat. Commun.* **2022**, *13*, 5698.
[10] S. Guo, S. C. Tan, *Joule* **2024**, *8*, 291.
[11] Y. Wang, W. Huang, S. Guo, X. Xin, Y. Zhang, P. Guo, S. Tang, X. Li, *Adv. Energy Mater.* **2021**, *11*, 2102452.
[12] C. Pornrungroj, A. B. Mohamad Annuar, Q. Wang, M. Rahaman, S. Bhattacharjee, V. Andrei, E. Reisner, *Nature Water* **2023**, *1*, 952.
[13] Z. Jiang, X. Zhang, G. Yang, Z. Yuan, X. Ji, F. Kong, B. Huang, D. D. Dionysiou, J. Chen, *Chem. Eng. J.* **2019**, *373*, 814.
[14] W. Zha, Q. Ruan, L. Kong, X. Xi, M. A. Turgunov, W. Zhang, K. Chang, Z. Sun, *Cell Rep. Phys. Sci.* **2022**, *3*, 100863.
[15] W. Lei, N. Suzuki, C. Terashima, A. Fujishima, *Front. Energy* **2021**, *15*, 577.
[16] K. Lee, Q. Kim, S. An, J. An, J. Kim, B. Kim, W. Jhe, *Proc. Natl. Acad. Sci. USA* **2014**, *111*, 5784.
[17] L. Yang, N. Feng, Q. Wang, Y. Chu, J. Xu, F. Deng, *Cell Reports Physical Science* **2020**, *1*, 100013.
[18] K. Shirai, T. Sugimoto, K. Watanabe, M. Haruta, H. Kurata, Y. Matsumoto, *Nano Lett.* **2016**, *16*, 1323.
[19] Y. Nosaka, A. Y. Nosaka, *Phys. Chem. Chem. Phys.* **2020**, *22*, 7146.
[20] D. Jeon, J. Park, C. Shin, H. Kim, J.-W. Jang, D. W. Lee, J. Ryu, *Sci. Adv.* **2020**, *6*, aaz3944.
[21] Q. Cao, B. Kumru, M. Antonietti, B. V. K. J. Schmidt, *Mater. Horiz.* **2020**, *7*, 762.
[22] C. Lang, J. A. LaNasa, N. Utomo, Y. Xu, M. J. Nelson, W. Song, M. A. Hickner, R. H. Colby, M. Kumar, R. J. Hickey, *Nat. Commun.* **2019**, *10*, 3855.
[23] H. Wang, L. Zhang, R. Chen, S. Guo, G. Sun, Q. Liu, J. Liu, J. Yu, P. Liu, J. Zhu, J. Wang, *Appl. Surf. Sci.* **2023**, *619*, 156527.
[24] R. Xie, J. Fan, K. Fang, W. Chen, Y. Song, Y. Pan, Y. Li, J. Liu, *Chemosphere* **2022**, *286*, 131541.
[25] W. Nie, M. Ruan, D. Guo, X. Liu, *Appl. Surf. Sci.* **2023**, *616*, 156415.
[26] L. Lin, Z. Yu, X. Wang, *Angew. Chem. Int. Ed. Engl.* **2019**, *58*, 6164.
[27] W. Li, Z. Lin, G. Yang, *Nanoscale* **2017**, *9*, 18290.
[28] Q. Luan, X. Xue, R. Li, L. Gu, W. Dong, D. Zhou, X. Wang, B. Li, G. Wang, C. Hou, *Appl. Catal., B* **2022**, *305*, 121007.
[29] M. Xiong, B. Chai, J. Yan, G. Fan, G. Song, *Appl. Surf. Sci.* **2020**, *514*, 145965.
[30] B. Lin, H. Li, H. An, W. Hao, J. Wei, Y. Dai, C. Ma, G. Yang, *Appl. Catal., B* **2018**, *220*, 542.
[31] Z. Xiang, H. Guan, B. Zhang, Y. Zhao, *J. Am. Ceram. Soc.* **2020**, *104*, 504.
[32] Z. Guan, J. Pan, Q. Li, G. Li, J. Yang, *ACS Sustain. Chem. Eng.* **2019**, *7*, 7736.
[33] P. Wang, Z. Shen, Y. Xia, H. Wang, L. Zheng, W. Xi, S. Zhan, *Adv. Funct. Mater.* **2019**, *29*, 1807013.
[34] W. Yang, L. Zhang, J. Xie, X. Zhang, Q. Liu, T. Yao, S. Wei, Q. Zhang, Y. Xie, *Angew. Chem. Int. Ed. Engl.* **2016**, *55*, 6716.
[35] G. Wang, Y. Liu, J. Zhang, Q. Chen, K. Fang, J. Mao, *J. Mater. Chem. A* **2022**, *10*, 21349.
[36] X. Jiao, Z. Chen, X. Li, Y. Sun, S. Gao, W. Yan, C. Wang, Q. Zhang, Y. Lin, Y. Luo, Y. Xie, *J. Am. Chem. Soc.* **2017**, *139*, 7586.
[37] X. Wang, X. Wang, J. Huang, S. Li, A. Meng, Z. Li, *Nat. Commun.* **2021**, *12*, 4112.
[38] W. Xu, W. Gao, L. Meng, W. Tian, L. Li, *Adv. Energy Mater.* **2021**, *11*, 2101181.
[39] Y. Fu, F. Cao, F. Wu, Z. Diao, J. Chen, S. Shen, L. Li, *Adv. Funct. Mater.* **2018**, *28*, 1706785.
[40] S. Yin, X. Zhao, E. Jiang, Y. Yan, P. Zhou, P. Huo, *Energy Environ. Sci.* **2022**, *15*, 1556.
[41] W.-K. Chong, B.-J. Ng, Y. J. Lee, L.-L. Tan, L. K. Putri, J. Low, A. R. Mohamed, S.-P. Chai, *Nat. Commun.* **2023**, *14*, 7676.
[42] C. Du, Q. Zhang, Z. Lin, B. Yan, C. Xia, G. Yang, *Appl. Catal., B* **2019**, *248*, 193.
[43] Y. T. Lin, S. N. Lai, J. M. Wu, *Adv. Mater.* **2020**, *32*, 2002875.
[44] C. Avcıoğlu, S. Avcıoğlu, M. F. Bekheet, A. Gurlo, *ACS Appl. Energy Mater.* **2023**, *6*, 1134.
[45] R. Yang, L. Mei, Y. Fan, Q. Zhang, R. Zhu, R. Amal, Z. Yin, Z. Zeng, *Small Methods* **2021**, *5*, 2100887.
[46] N. Hu, W. Wang, L. Lei, H. Fan, Y. Tan, H. Yuan, Z. Mao, P. Müller-Buschbaum, Q. Zhong, *Green Chem.* **2021**, *23*, 8969.
[47] Y. Zhou, Y. Zhang, L. Zhang, J. Qiu, J. Yao, *Carbohydr. Polym.* **2023**, *312*, 120845.
[48] S. J. Bégin, K. M. Scotland, P. R. Pede, A. J. Vreugdenhil, *Macromol. Chem. Phys.* **2023**, *224*, 2300223.
[49] Y. Ma, G. Hai, D. G. Atinafu, W. Dong, R. Li, C. Hou, G. Wang, *J. Colloid Interface Sci.* **2020**, *569*, 89.
[50] S. Wang, P. Li, L. Sheng, L. Z. Song, R. Zang, S. S. Liu, L. Q. Liu, W. Zhou, *Catal. Sci. Technol.* **2022**, *12*, 927.
[51] J. Y. Li, X. Y. Du, X. X. Wang, X. Y. Yuan, D. H. Guan, J. J. Xu, *Angew. Chem. Int. Ed. Engl.* **2024**, *63*, 202319211.
[52] Q. Ran, Z. B. Yu, R. H. Jiang, L. Qian, Y. P. Hou, F. Yang, F. Y. Li, M. J. Li, Q. Q. Sun, H. Q. Zhang, *Catal. Sci. Technol.* **2020**, *10*, 2531.
[53] J. Chen, H. Zhang, P. Liu, Y. Li, X. Liu, G. Li, P. K. Wong, T. An, H. Zhao, *Appl. Catal., B* **2015**, *168*, 266.
[54] K. Wang, D. Y. Liu, L. M. Liu, J. Liu, X. F. Hu, P. Li, M. T. Li, A. S. Vasenko, C. H. Xiao, S. J. Ding, *eScience* **2022**, *2*, 518.
[55] D. Li, Y. Zhao, C. Zhou, L. P. Zhang, J. Tang, T. Zhang, *Fundam. Res.* **2024**, *4*, 934.
[56] Y. Peng, X. Guo, S. Xu, Y. Guo, D. Zhang, M. Wang, G. Wei, X. Yang, Z. Li, Y. Zhang, F. Tian, *J. Energy Chem.* **2022**, *75*, 276.
[57] H. Liu, R. Suo, W. Li, L. Luo, H. Yang, J. Chen, C.-Z. Lu, *Sep. Purif. Technol.* **2024**, *346*, 127439.
[58] P. Zhang, X. Yin, D. Zhang, P. Guo, W. Liu, R. Wang, Z. Zhang, S. Qiu, *Chem. Eng. J.* **2023**, *458*, 141394.
[59] Q. Li, H. Yue, C. Liu, K. Ma, S. Zhong, B. Liang, S. Tang, *Chem. Eng. J.* **2020**, *395*, 125120.
[60] T. Tian, X. Jin, N. Guo, H. Li, Y. Han, Y. Yuan, *Appl. Catal., B* **2022**, *308*, 121227.
[61] W. H. Lee, C. W. Lee, G. D. Cha, B.-H. Lee, J. H. Jeong, H. Park, J. Heo, M. S. Bootharaju, S.-H. Sunwoo, J. H. Kim, K. H. Ahn, D.-H. Kim, T. Hyeon, *Nat. Nanotechnol.* **2023**, *18*, 754.
[62] X. Xin, Y. Zhang, R. Wang, Y. Wang, P. Guo, X. Li, *Nat. Commun.* **2023**, *14*, 1759.
[63] S. Guo, X. Li, J. Li, B. Wei, *Nat. Commun.* **2021**, *12*, 1343.
[64] L. He, X. Zeng, H. Chen, L. Zhao, Z. Huang, D. Wang, X. He, W. Fang, X. Du, W. Li, *Adv. Funct. Mater.* **2024**, *34*, 2313058.
[65] W. Zhou, H. Huang, Z. Wang, S. W. Sharshir, C. Wang, M. An, L. Wang, Z. Yuan, *J. Mater. Chem. A* **2024**, *12*, 4046.
[66] X. Zhou, F. Zhao, Y. Guo, B. Rosenberger, G. Yu, *Sci. Adv.* **2020**, *5*, aaw5484.
[67] L. X. Hou, H. Ju, X. P. Hao, H. Zhang, L. Zhang, Z. He, J. Wang, Q. Zheng, Z. L. Wu, *Adv. Mater.* **2023**, *35*, 2300244.
[68] Y. Zhang, C. Chen, Y. Chen, Y. Chen, *Food Hydrocolloids* **2019**, *91*, 136.
[69] B. Liu, Y. Zhao, Y. Li, L. Tao, P. Pan, Y. Bi, S. Song, L. Yu, *Int. J. Biol. Macromol.* **2024**, *263*, 130277.
[70] J. Ren, L. Chen, J. Gong, J. Qu, R. Niu, *Chem. Eng. J.* **2023**, *458*, 141511.
[71] Z. Fang, S. Tang, Z. Wang, M. An, G. Yu, *ACS Cent Sci.* **2022**, *8*, 627.
[72] K. Sano, N. Igarashi, Y. Ebina, T. Sasaki, T. Hikima, T. Aida, Y. Ishida, *Nat. Commun.* **2020**, *11*, 6026.